Geophysical imaging of regolith in landscapes along a climate and vegetation gradient in the Chilean Coastal Cordillera

Igor Dal Bo[1]

Anja Klotzsche[1]

Mirjam Schaller[2]

Todd Alan Ehlers[2]

Manuela S. Kaufmann[1]

Juan Pablo Fuentes Espoz[3]

Harry Vereecken[1]

Jan van der Kruk[1]

[1] Agrosphere (IBG-3), Institute of Bio- and Geosciences, Forschungszentrum Jülich GmbH, Wilhelm-Johnen-Straße, 52428, Juelich, Germany

[2] Department of Geosciences, University of Tuebingen, Wilhelmstrasse 56, 72074 Tuebingen, Germany

[3] University of Chile, Department of Silviculture and Nature Conservation, Av. 14 Santa Rosa 11315, La Pintana, Santiago RM, Chile

Corresponding author: Igor Dal Bo (i.dal.bo@fz-juelich.de)

ABSTRACT

Many studies have recently shown the potential of geophysical tools in bridging the information gap between individual point-scale measurements. Here, we upscale and extend the point-scale layering information from pedons (excavated pit of 1 m^2) using geophysical methods. We applied multi-frequency ground-penetrating radar (GPR) in four study areas in the extreme climate and vegetation gradient of the Chilean Coastal Cordillera. The main goals of this study were to understand how granitic based regolith material varies depending on climate, vegetation cover, aspect, and topography.

GPR was successfully used in all four study areas. Reflections, which were imaged up to a depth of 8 m, could be associated with boundaries visible in the pedons. The main recognizable reflections were linked with the interface between the mobile soil and the immobile saprolite. This boundary is characterized by hyperbolic-shape features, probably connected to heterogeneities (e.g. pebbles). A deeper GPR penetration depth in south-facing hillslopes was observed than in north-facing hillslopes. This is probably due to less sun exposure in the south facing slopes, which results in higher soil water content and denser plant growth, facilitating weathering processes. Furthermore, thicker layers in the GPR profiles are visible going from north to south along the latitude. Most of these observations were in agreement with the soil pedons.

These results demonstrate the utility of the GPR technique for characterizing subsurface variations in regolith properties (e.g. thickness, boundaries). Additional soil pedons should be excavated based on GPR results. Applying noninvasive geophysical methods could improve the understanding of the interactions between soil formation, vegetation, and other environmental parameters.

Keywords: ground-penetrating radar; geophysical imaging; granitic regolith; hillslope aspect; weathering processes.

1. INTRODUCTION

The decomposition of rock by physical erosion and chemical weathering is driven by tectonic, climatic, and biological processes. The thickness of the weathered rock material and the degree of weathering are influenced by time, the type of parent material, topography, climate, and hence biota (Jenny, 1994). The direct investigation of the extent and degree of regolith is restricted to excavated soil pedons, augers, and drilling of boreholes. Point observations are not only time consuming and expensive but provide little information about the spatial variation of regolith in a landscape. These point observations can be combined with non-invasive tools such as geophysics to gain more spatial coverage (Beauvais et al., 2004; De Benedetto et al., 2012).

Geophysical techniques like electrical resistivity tomography (ERT), electro-magnetic induction (EMI), ground-penetrating radar (GPR), and seismic have been widely applied to classify soil properties (Breiner et al., 2011; Dominic et al., 1995; Novakova et al., 2013) and soil and rock stratigraphy (Afshar et al., 2017; Befus et al., 2011; Brandt et al., 2007; Davis and Annan, 1989; Dominic et al., 1995; Parsekian et al., 2015; van Overmeeren, 1998; Zaremba et al., 2016). GPR was successfully applied in karst areas to recognize shallow regolith layering and bedrock (Estrada-Medina et al., 2010; Fernandes et al., 2015). GPR has been combined with EMI, showing how the effectiveness of the two methods is strongly dependent on the electrical properties of the soil (Doolittle and Collins, 1998). Carrière et al. (2013) coupled ERT and GPR techniques for the geological characterization of karst media. Similarly, the thickness of the weathering horizons was determined using ERT and GPR in a two-stepped lateritic regolith (Beauvais et al., 2004). This roughly corresponded to the thickness measured in

boreholes, which showed significant lateral variability (Beauvais et al., 1999). GPR has also been used in sub-humid tropic areas to analyze and obtain indirect geological, geomorphological, and pedological information about regolith with a relatively high degree of detail (Aranha et al., 2002). The combination of GPR and borehole observations revealed the influence of lithology on weathering processes, where laterally discontinuous zones of fractures were shown hosting corestones and colluvial material (Orlando et al., 2016). The combination of seismic refraction and ERT with observations from road cuts revealed that the interaction between tectonic stress and topography influences the depth of the critical zone, and thus the regolith formation (Holbrook et al., 2014; St. Clair et al., 2015).

The combination of geophysical techniques with field observations and geochemical data for regolith characterization has shown a large potential to investigate spatial variability of weathered rock and parent material at the hillslope scale (Braun et al., 2009; Breiner et al., 2011). Furthermore, GPR, EMI, and ERT techniques have been successfully applied to retrieve information about soil layering and properties (André et al., 2012; Busch et al., 2013). However, the combination of several geophysical methods has not been tested for characterizing variations in regolith related to changes in climate and biota. Whereas geophysical methods cannot directly measure the degree of weathering (a chemical and biologic process), they can identify spatial variations in physical properties caused by weathering processes. Thus, layering differences sensed by geophysical methods provide a proxy for subsurface variations in regolith.

In this study, we applied a multi-frequency GPR method in combination with observations from pedons (the smallest volume that can represent soil horizons and

properties variability, see Soil Survey Staff (1999)) to characterize variations in the soil and saprolite layer thicknesses. Four study areas along the climate and vegetation gradient of the Chilean Coastal Cordillera have been investigated (Fig. 1). These study areas were chosen because of their pronounced latitudinal variations in climate and vegetation, but similar parent material (i.e. granitic) and tectonic setting. We address the following questions:

1) how does regolith vary within a single hillslope;

2) how does regolith vary in hillslopes of the same area but with different aspects (e.g., north- and south-facing hillslopes); and

3) how does regolith vary in different climate settings?

2. STUDY AREAS AND PEDON INFORMATION

In the framework of the DFG-SPP Program 1803 project EarthShape (2016) four study areas located in the Chilean Coastal Cordillera (Fig. 1) with latitudes ranging from 26°S to 38°S were selected. These areas include from north to south: Parque Nacional Pan de Azúcar, Reserva Santa Gracia, Parque Nacional La Campana, and Parque Nacional Nahuelbuta (Fig. 1b and c). In these areas, the climate changes from desert to arid, Mediterranean, and humid conditions from north to south. We retrieved mean annual precipitation (MAP) and temperature (MAT) for the pedon locations from the model of Karger et al. (2017), which is based on the reanalysis of the data assimilation model ERA-Interim (Dee et al., 2011). This simulates temperature and precipitation using ground, radiosonde, and remote sensing observations, downscaling the final result at a resolution of 100 m. Going from north (Pan de Azúcar) to south (Nahuelbuta),

we derived MAT of 20.1º, 15.1º, 14.9º, and 12.9 º C, and MAP of 15, 77, 326, and 1050 mm, respectively (Karger et al., 2017). Average soil thickness for the four study areas was retrieved from Bernhard et al. (2018) and Oeser et al. (2018). The bulk rock composition is comparable in all four sites and can be defined as a granitic lithology (Charrier et al., 2015; Sernageomin, 1982). Going from south to north, older rocks can be found spacing from Carboniferous to Cretaceous in age (Sernageomin, 1982). No influence by Alpine glaciers and last glacial maximum (LGM) glaciation is reported in the four study areas (Rabassa and Clapperton, 1990). The calculated tectonic uplift is 0.2±0.1 mm yr^{-1} (Kukowski and Oncken, 2006).

2.1. Pan de Azúcar

Parque Nacional Pan de Azúcar (~26°S and 71°W) is located in the south-westernmost branch of the Atacama Desert. It is classified as an arid desert zone. The streams in this region are ephemeral and rarely have water in them, except during seldom rainstorms. Vegetation is mostly observed in the coastal area and sustained by fog (Lehnert et al., 2018). Instead, in the pedons' area vegetation is only sparsely present in the valley bottoms (gullies) and absent on crests. The main lithology comprehends tonalites, diorites, granodiorites, monzodiorites, and gabbros (Fuentes et al., 2016; Sernageomin, 1982). Many basaltic dykes are present crossing the granitic material. Fewer amounts of argillite and andesite can be found in the area as well. Soil is thin and has an average thickness of 0.20 m (Table 1, Bernhard et al., 2018; Oeser et al., 2018).

2.2. Santa Gracia

Reserva Santa Gracia (~29°S and 71°W) is classified as transitional from arid to semi-arid/Mediterranean climate zone. Vegetation is represented by shrubs and cacti and sustained by fog (Arroyo et al., 1993). The lithology is mainly composed of tonalities, diorites, monzodiorites, granodiorites, and monzogranites (Sernageomin, 1982). The interface between soil and saprolite ranges from 0.35 to 0.60 m (Table 1, Bernhard et al., 2018; Oeser et al., 2018).

2.3. La Campana

Parque National La Campana (~32° and 71°W) has a semi-arid/Mediterranean climate and the vegetation is mainly represented by palm trees, bushes, and evergreen sclerophyllous plants (Table 1, Arroyo et al., 1993; Di Castri et al., 1981; González et al., 2009; Zunino and Saiz, 1991). The lithology is made of diorites, monzodiorites, granodiorites, and monzogranites (Sernageomin, 1982). The soil has an average thickness of 0.40 to 0.60 m (Table 1, Bernhard et al., 2018; Oeser et al., 2018).

2.4. Nahuelbuta

Parque Nacional Nahuelbuta (~38° and 73°W) is classified as a humid temperate zone without dry season. Water flows permanently in the streams. As a result of this type of climate, the park is characterized by dense vegetation which comprehends extensive remains of pristine temperate Araucaria forests (Table 1, Cisternas et al., 1999). The parent material is mainly made of granites, granodiorites, tonalities, and diorites (Sernageomin, 1982). In the southern side of the park metamorphic rocks are

164 present, such as metasandstones, philites, marbles, metabasalts, and
165 metaconglomerates (Sernageomin, 1982). The thickness of the soil ranges between
166 0.70 and 1.00 m (Table 1, Bernhard et al., 2018; Oeser et al., 2018).
167
168 **2.5. Pedon information**
169 Several pedons have been described (Table 1) for the four study areas as shown in
170 Fig. 1 (Bernhard et al., 2018; Oeser et al., 2018). In the south-facing slopes at least
171 three pedons were excavated along a transect (top-, mid-, and toe-slope), whereas only
172 one was excavated in the north-facing mid-slopes as cross-check for aspect-related
173 differences (Oeser et al., 2018). In this study, we have taken into account only the
174 regolith layering visible in the pedons as a direct link between ground truth data and
175 geophysical data (Scott and Pain, 2009). The main master horizons have been
176 identified as O, A, B, and C horizons, where O, A, and B horizons are called soil and the
177 weathered C horizon saprolite (Soil Survey Staff, 1996). Specific emphasis was put in
178 the boundary between B and C horizons as the variation from mobile soil materials to
179 immobile saprolite could result in a dominant physical contrast (Beauvais et al., 2004).
180 Inner-horizon layering (e.g. A and B horizons, saprolite) was also considered as this
181 might produce a significant contrast identifiable by geophysical methods. Moreover, the
182 bottom boundary of each pedon was taken into account, as it could produce significant
183 variations in the material properties detectable by geophysical methods. It was planned
184 to excavate all the pedons up to 2.00 m depth. However, in most cases (e.g. Pan de
185 Azúcar, Santa Gracia, La Campana) a transition towards unfractured rock was reached
186 before 2.00 m that made deeper excavation difficult.

187

188 ## 3. GEOPHYSICAL METHODS

189 In each study area, GPR common offset (CO) measurements were conducted at the
190 profile scale, whereas at the point-scale GPR wide-angle reflection-refraction (WARR)
191 were measured. The covered areas in the four study sites were restricted due to a
192 combination of dense vegetation and steep slopes.

193

194 ### 3.1. Multi-frequency Ground-penetrating Radar (GPR)

195 GPR is based on the propagation of electromagnetic (EM) waves. A typical on-
196 ground GPR is assembled with transmitting (Tx) and a receiving (Rx) antennae.
197 Whenever a contrast in the physical parameters of the subsurface is present, the EM
198 signal is reflected and scattered, and measured by the receiving antenna (Jol, 2008).

199 The material properties that influence the GPR applications are the relative dielectric
200 permittivity ε_r, the electrical conductivity σ , and the magnetic permeability μ, which is
201 often simplified to the value of the free space and it has seldom an influence on the EM
202 wave propagation. However, ε_r and σ have a stronger influence on the signal and are
203 associated to two key wave field properties that are the velocity v and the attenuation α,
204 respectively. Generally, α is a combination of electrical losses and scattering losses,
205 both of which increase with enhanced frequency (Jol, 2008). Thus, with a high
206 frequency a shallower penetration and a higher resolution are obtained (for constant
207 attenuation of the EM wave). The transmitting antenna generates a signal characterized
208 by a certain central frequency f_c that is directly related to the wavelength of the emitted
209 signal λ (Jol, 2008).

210 The most common way of measuring with GPR consists in using a single transmitter
211 and receiver, where the distance (offset) between the antennae can be fixed or variable.
212 In the first case, a common offset (CO) profile is measured, with the goal of mapping
213 subsurface reflectivity versus spatial position. A topographic correction might be
214 necessary in the cases of sensible elevation changes (Heincke et al., 2005). In the
215 second case, a common midpoint (CMP) or wide-angle reflection-refraction (WARR)
216 survey is measured, with the goal of estimating the velocity of the EM wave and the
217 relative dielectric permittivity ε_r, analyzing the recorded signal with a semblance
218 approach (Jacob and Urban, 2016; Tillard and Dubois, 1995; van der Kruk et al., 2010;
219 Yilmaz, 2001).
220
221 **3.2. Data acquisition**
222 Within each study area, we measured 10 to 100 m transects going from the toe to the
223 top of the hillslopes deploying GPR and using the excavated pedons as reference
224 points (see Fig. 1, green lines and red stars, respectively). At these locations, WARRs
225 were measured if possible (see Fig. 1, yellow circles). Whereas steepness was the main
226 factor limiting the surveyed length in Pan de Azúcar, denser vegetation towards
227 southern latitudes was also a limitation. The GPR surveys were carried out using the
228 pulseEKKO system (Sensors&Software, Mississauga, Canada), with several antennae
229 having a central frequency in air of 100, 200, 500, and 1000 MHz. The 100 and 200
230 MHz antennae were unshielded and mainly used stepwise, whereas the 500 and 1000
231 MHz were shielded and employed using a sledge and an odometer as trigger, with a
232 step size between 0.02 and 0.1 cm. The sampling rate of GPR measurements

233 depended on the used frequency (Jol, 2008) and varied between 0.2 and 0.4 ns. The
234 GPR systems were equipped with a Novatel GPS with a maximum horizontal precision
235 of 2 m.
236
237 **3.3. Data processing**
238 GPR and WARR data were processed using Matlab. A novel combined linear move-
239 out (LMO) – hyperbolic move-out (HMO) semblance analysis approach was developed
240 for analyzing CMP/WARR data (Fig. 2, see Fig. 1c for the position). LMO is carried out
241 for small travel times and can be used to estimate the velocity of the ground wave – the
242 direct wave travelling through the first few centimeters of the subsurface (Fig 2a). HMO
243 is carried out for large travel time and can be used to estimate the velocity of reflections
244 (Fig. 2a). This procedure is performed for a range of velocities ($0.05 < v < 0.3$ m ns^{-1})
245 and times by calculating the semblance (Heincke et al., 2006) over a window T
246 $$T = 1.2 \cdot \left(\frac{1}{f_c}\right), \quad (1)$$
247 where f_c is the nominal antennae frequency.
248 High values of semblance (warm colors, Fig. 2c) indicate velocities of ground wave
249 and reflections (Fig. 2b), which can be used for the time-to-depth conversion and for the
250 calculation of physical parameters of the subsoil (e.g. permittivity). The selected
251 waveforms within the semblance window are shown in Fig. 2d and e for the LMO
252 corrected groundwave and the HMO corrected reflected wave, respectively. The highest
253 alignment in Fig. 2d and e is obtained when the signal after correction is mostly
254 horizontal. To compare pedon interfaces and WARR reflections, depths (Table 1) were
255 converted into travel times using the average ground wave velocity for each location

256 (Table 2). The theoretical hyperbola produced by each interface was calculated using a
257 weighted velocity for each WARR.
258 GPR CO data were processed following a standard routine: dewow filter, time-zero
259 correction, frequency domain butterworth filter, energy decay gain, and time-to-depth
260 dynamic conversion using the calculated average velocity for each location (Jol, 2008).
261 In some cases (e.g. noisy 1000 MHz profiles) we applied an average removing filter for
262 the ringing, as described by Kim et al. (2007). We extended the amplitude analysis
263 calculating instantaneous attributes of common-offset profiles (Gross et al., 2003). In
264 particular, the instantaneous amplitude (envelope) resulted to be a valuable tool to
265 enhance interpretation, as it gave a quantitative estimation of the subsoil reflectivity
266 (Forte et al., 2012; Gross et al., 2003; Zhao et al., 2013).
267
268 **4. RESULTS**
269 We present in the following subsections GPR CO and WARR geophysical results of
270 the four study areas (see Fig. 1c for the measured data positions). Sometimes, the
271 measurements couldn't be carried out due to logistical problems. Where possible,
272 profiles were gathered to investigate the crossline -variability within a specific hillslope
273 (e.g. Santa Gracia and La Campana in Fig. 1).
274
275 **4.1. Pan de Azucar geophysical results**
276 An average ground wave velocity of 0.147 m ns^{-1} was obtained from WARR
277 measurements (Table 2). In addition, a reflection was present in the north-facing
278 hillslope (WARR of Fig. 1c) at a travel time of 9 ns indicating a velocity of 0.121 m ns^{-1}

279 that is probably related to an interface at 0.45 m within the saprolite layer (see Table 1
280 and Fig 3, blue dot).

281 GPR profiles were measured with 500 MHz and 1000 MHz central frequency
282 antennae for 8 m along the north-facing mid pedon (Fig. 3, see Fig. 1c for the position).
283 The pedon bottom boundary at 1.10 m (green arrows in Fig., 3, see also Table 1) can
284 be linked with reflections in both 1000 MHz (Fig. 3a) and 500 MHz (Fig. 3b) CO profiles
285 measured on north-facing hillslopes. This reflection is visible between the position of 2
286 and 4 m and 7.5 and 8.5 m (Fig. 3a and b) and characterized by strong reflectivity in the
287 envelope profile (Fig. 3c, black ellipses). On the contrary, reflections connected with
288 inner saprolite layering at 0.45 m (blue arrows, Table 1) appear to be nearly horizontal
289 between position of 3 and 7 m and closing with an unconformity on the reflector linked
290 with the pedon bottom boundary. The reflector linked with the boundary mobile soil to
291 immobile saprolite at 0.20 m can be followed in the position between 3 and 5 m along
292 the profile (red arrows, Fig. 3a and Table 1).

293 A 1000 MHz antennae GPR profile was measured along toe and mid pedon positions
294 for 11 m in the south-facing hillslope (Fig. 4, see Fig. 1c for the position). GPR CO data
295 towards the south-facing top pedon were not measured due to a steep slope and
296 unstable loose material on the surface. No clear continuous reflection could be
297 identified, although between the position of 8 and 9 m an upwards dipping reflector is
298 visible and linked with inner saprolite layering at about 0.55 m (blue arrows, Table 1).
299 Insights of GPR signal penetration depth are highlighted in the reflection strength (Fig.
300 4b), where deeper high-reflectivity values were obtained in the mid slope and shallower
301 in the toe slope (red line).

302

303 **4.2. Santa Gracia geophysical results**

304 WARRs with 500 and 1000 MHz GPR antennae were measured at each pedon
305 position (Fig. 1c) and an average ground wave velocity value of 0.153 m ns^{-1} was
306 obtained (Table 2). A decreasing gradient of ground wave velocities was determined at
307 the south-facing hillslope going uphill: 0.162 m ns^{-1} at the toe, 0.151 m ns^{-1} at the mid
308 and 0.147 m ns^{-1} at the top slope. Ongoing soil core investigations are necessary to
309 understand this gradient. A ground wave velocity of 0.159 m ns^{-1} was obtained for the
310 north-facing slope. When reflections were present, a rather constant velocity value of
311 0.130 m ns^{-1} was calculated between a depth of 0.80 and 1.50 m, probably indicating a
312 transition towards a more homogeneous and compacted medium.

313 Several 500 MHz GPR profiles were measured going uphill over south- and north-
314 facing hillslopes in Santa Gracia study area (Fig. 1c). Portions of the GPR CO over the
315 north-facing mid slope (Fig. 5a), south-facing toe (Fig. 5b), mid (Fig. 5c), and top (Fig.
316 5d) slopes are shown here, alongside with their envelopes (see Fig. 1c for the exact
317 locations). No reflections are visible in the profile in the north-facing slope and signal
318 penetration is shallow (about 10 ns or 0.4 m). Deeper reflectors are visible in the south-
319 facing slope, where hyperbolic features are identifiable up to a travel time of 30 ns (~2.5
320 m). In particular, they are linked with inner saprolite layering at 0.80 m in toe and at 0.75
321 m in mid slope and with the boundary mobile soil-immobile saprolite at 0.35 m in the top
322 slope (Table 1). Hyperbolas are highlighted by the envelope profiles, being less present
323 towards the top slope, where also signal penetration is shallower (Fig. 5d).

324

4.3. La Campana geophysical results

WARRs were measured at the bottom of the south-facing hill due to difficulties in measuring along the slope (Fig. 1c), by which an average value of 0.134 m ns^{-1} was obtained for the ground wave velocity (Table 2).

Hyperbolas are the main features visible in GPR CO profiles of La Campana study area, indicating a rather heterogeneous subsurface. In particular, these features can be seen in Fig. 6, where four 500 MHz GPR CO cross- and inlines were measured over an 11 m x 11 m area at the south-facing mid slope (see rectangle in Fig.1c for the position). The pedon layers were projected accordingly to the semi-3D volume (Fig. 6). The boundary between B horizon and saprolite at 0.60 m (Table 1) was linked to the presence of hyperbolic features on crossline 1, inline 1, and inline 2. Two continuous reflections of about 5 m are present on crossline 2 (Fig. 6, cyan dashed lines) that are linked to the boundary between A and B horizon, and B horizon and saprolite, at 0.30 and 0.60 m depth respectively (Table 1). The transition mobile to immobile soil appeared at a rather constant depth (0.40 to 0.60 m) in the whole area and was characterized by heterogeneities, with a slightly thicker mobile soil in the south-facing mid slope (Table 1).

4.4. Nahuelbuta geophysical results

At each pedon location a WARR was measured (Fig. 1c) and an average value of ground wave velocity of 0.115 m ns^{-1} was obtained (Table 2). Reflections were present both in the 500 MHz WARR (Fig. 2b, see Fig. 1c for the position) and 200 MHz WARR (Fig. 7a) measured in the south-facing mid pedon. Hyperbolic features were found at

348 the same travel time as the high-amplitude reflectors in the respective GPR CO profiles
349 (Fig. 7b and 8a). In particular, the reflection at 34 ns is consistent with the depth of the
350 bottom of the south-facing mid pedon at 2.04 m (Table 1) in both WARRs (Fig. 2 and
351 7a). No clear reflections were linkable with toe and top pedons in the respective
352 WARRs, although high energy patches in the semblance analysis could be related to
353 hyperbolic features in the CO profiles.

354 Fig. 7 and 8 show 500 and 200 MHz GPR CO profiles, respectively, measured at the
355 south-facing mid pedon, which is located at the position of 3 m along the profiles. Two
356 high amplitude reflectors are recognizable that are linked with the pedon layering. The
357 reflector linked with the pedon bottom boundary at 2.04 m shows lateral variability and
358 high reflectivity in the envelope profile (green arrows, Fig. 8a and b, and Table 1). It is
359 nearly horizontal in the positions between 0 and 15 m, whereas it dips upwards from 40
360 (~2 m) to 20 ns (~1 m) between the positions of 15 and 32 m. The same reflection could
361 be related to an inner saprolite layering in the south-facing top pedon at about 90 cm
362 (Table 1). This reflection at 34 ns (~2 m) is also visible in the 200 MHz CO profile (Fig.
363 7b), which covers the first 12 m of transect in Fig. 8. Hyperbolic features enhanced by
364 the envelope are present between 7 and 18 ns (0.40 to 0.80 m) in the 500 MHz CO
365 profile (Fig 8a) that are probably indicating heterogeneities within the B horizon (Table
366 1). These are imaged as a continuous reflection between 20 and 30 ns (1 to1.5 m
367 depth) in the 200 MHz CO profile (Fig. 7b). Here, deeper structures are visible at about
368 100 - 120 ns (5 to 7 m, Fig. 7b). To identify whether these reflections were coming from
369 objects above the surface (van der Kruk and Slob, 2004), we analyzed the WARR
370 measurements to exclude that the reflections were travelling with the speed of air.

371 At the north-facing hillslope, a 6 m long GPR profile was gathered (Fig. 1c) that
372 showed undulated reflections at about 0.40 m linked with the interface between A and B
373 horizon (Table 1). A further down-dipping reflection was linked with the boundary
374 between B horizon and saprolite at about 0.90 m. A WARR measured at the pedon
375 location confirmed the presence of semi-continuous reflections with lateral variations.
376
377 ### 4.5. GPR envelope-based observation
378 To compare the GPR data measured at all sites and slopes, the calculated envelopes
379 from 500 MHz GPR profiles were averaged for transects of similar length (about 10 m)
380 for the four study sites on the north- and south-facing mid slopes (Fig. 9). The signal-to-
381 noise threshold, indicating the maximum travel time and penetration depth, was
382 calculated for each curve regarding the interval between 55 and 60 ns as noise. This
383 value was multiplied by 3 (obtained value after estimation of best signal-to-noise
384 approximation for all the envelopes) and the intercept with each envelope curve was
385 calculated and shown in Table 2. Except for Pan de Azucar, the envelope curves
386 showed larger maximum travel time - and consequently increasing penetration depth -
387 at the south-facing slopes compared to north facing slopes (Table 2). In addition, larger
388 maximum travel time and deeper penetration depths could be observed from north to
389 south in latitude (Table 2), except for Pan de Azucar.
390
391 ## 5. DISCUSSION
392 ### 5.1. General findings

393 Four different reflection patterns could be identified from GPR CO profiles (Fig. 10a):
394 continuous reflections, discontinuous reflections, hyperbolic features, and zones where
395 no clear reflections could be seen. These were constrained and validated by WARRs
396 measured at the soil pedon key locations (Fig. 1c). Continuous reflections in GPR CO
397 profiles were associated with clear continuous hyperbolas on WARRs. Discontinuous
398 reflections were seen as fragmented hyperbolic trajectories on WARRs, still producing
399 high semblance values. Hyperbolic features were imaged as chaotic and fragmented
400 hyperbolic trajectories, not generating large values of semblance. Where no clear
401 reflection was visible, the GPR signal looked similar both in GPR CO profiles and
402 WARRs (Fig. 10b).
403 We extracted the GPR facies defined in Fig. 10 from 1000, 500, and 200 MHz CO
404 profiles across the studied hillslopes. These have been combined with approximate
405 elevation profiles and pedon layering, plotted accordingly to Table 1 using a specific
406 color code (Fig. 11, Orlando et al., 2016; van Overmeeren, 1998). In some cases,
407 pedons were vertically exaggerated to enhance visibility of the layers and overcome the
408 1:1 scale used for the topographic data (Fig. 11b, d, f, g, and h). Deploying GPR
409 systems with different frequencies over the same transects helped identifying common
410 reflections at specific depths, reaching a relatively high degree of detail in the definition
411 of the regolith layering and of pedological processes (Aranha et al., 2002). A maximum
412 horizontal precision of 2 m was reached measuring topographic data during the first
413 campaign due to the GPS system; hence, preliminary DGPS high-precision data (max 3
414 cm horizontally) from a second measurement campaign have been used to improve the
415 topography. Still, particularly in vegetated environments (La Campana and Nahuelbuta,

Fig. 11e, f, g, and h), positioning artifacts are sparsely present that were smoothed by a moving average filter.

The interface between A and B horizons could be linked with continuous reflections on 500 MHz GPR CO profiles only in the two southernmost locations, La Campana and Nahuelbuta (Fig 11f and h, respectively). This was not possible in the two northern study areas as this boundary is usually shallow and not detectable by the used GPR systems. Deploying higher frequencies systems (1.6 GHz and 2.6 GHz) could possibly enhance the detectability of the shallower layers. High-amplitude reflections from 500 and 1000 MHz GPR CO profiles at the four locations were mainly linked with the boundary between B horizon and saprolite, which produced distinct amplitude variations when present (Beauvais et al., 2004). This interface is often represented by hyperbolic features, making the interpretation more challenging and less straightforward (Aranha et al., 2002). Hyperbolas are generated when subsurface heterogeneities form a sensible contrast in ε_r relatively to the surrounding medium. The frequency dependent dominant wavelength of the emitted wave plays an important role on the resolution and size of the objects that can be sensed. Whereas high frequencies show undulated reflections and individual features from which the interfaces are being built up (e.g. Fig. 8a), low frequencies have reduced resolution and show a more continuous interface (Fig. 7b). We believe that in this case hyperbolic features on GPR CO profiles are generated by pebbles and fractured blocks having dimensions in the order of the dominant wavelength of 500 and 1000 MHz GPR antennae (5 to 25 cm, Table 2), as it was reported in the description of the pedons (Bernhard et al., 2018; Oeser et al., 2018, see Table 1). Furthermore, corestones were visible on outcrops in this study areas

(Hewawasam et al., 2013; Oeser et al., 2018) that could generate such a contrast in the electromagnetic properties (Orlando et al., 2016). Such signals could also be generated in La Campana and Nahuelbuta study areas by the presence of roots, although the maximum reported root diameter for the two sites is 5 cm (Oeser et al., 2018, see Table 1), which is too small for the deployed frequencies (Butnor et al., 2001; Hirano et al., 2009). Inner saprolite layering and pedon bottoms were mainly imaged as continuous reflections on 500 and 1000 MHz GPR CO profiles, as it is for examples in Pan de Azucar north-facing hillslope and Nahuelbuta south-facing hillslope (Fig 11a and h, respectively). In only one situation no clear reflection patterns were identifiable by GPR measurements (Santa Gracia north-facing hillslope, Fig. 5a and 11c), which is probably related to the presence of homogeneous media and/or to a shallow saprolite interface. Denser soil coring and sample analyses (e.g. texture, soil water content, OC, EC_{eff}) would help understanding the detected GPR signals in the four study areas.

5.2. Changes within a hillslope

Beauvais et al. (1999), Befus et al. (2011), and Holbrook et al. (2014) showed that the thickness of regolith is decresing from about 35 m at the center of the catchment to about 5 m at the top of the slope. Compressional seismic wave velocity (*Vp*) and ERT were deployed over profiles of 200 to 1300 m, showing high lateral variability and thickness variations up to tens of meters. Similarly, our observations from GPR at a smaller scale (5 to 200 m CO profiles) indicate that the target regolith layers are found at deeper depths (between 0.40 and 2 m) in the toe – mid slopes than in the top slopes (between 0.30 and 1 m), probably because of gravitational effects (Walker and Ruhe,

1968). However, whereas Beauvais et al. (1999), Befus et al. (2011), and Holbrook et al. (2014) focused on imaging the deep regolith and the interface with the bedrock, we focused on the first 3 to 5 m of the subsurface.

We were able to image vertical variations of GPR reflection thickness that could be roughly linked with interfaces (e.g. A, B horizons, and saprolite) visible in the pedons (Table 1) and extrapolated to the profile scale for tens of meters (Fig. 11, Beauvais et al., 2004).

5.3. Variations between south- and north-facing hillslopes

Befus et al. (2011) found deeper interfaces (up to 4 m) on north-facing slopes than on south-facing slopes in the northern hemisphere within the critical zone in terms of compressional seismic velocity *(V_p)*. Here, in the southern hemisphere we similarly observe larger penetration depths of GPR reflections (up to 0.80 m) for south-facing hillslopes compared to north-facing hillslopes (Table 2). These observations are consistent with the soil pedons (Bernhard et al., 2018, see Table 1). This smaller difference if compared with Befus et al. (2011) is probably related to the higher mobility of the upper regolith layer and/or to different stages of soil development in the study areas (Bernhard et al., 2018). We believe that aspect-driven differences could reflect lower temperature and greater soil moisture retention of the south-facing slopes due to denser vegetation and less sun radiation (Anderson et al., 2013; Rech et al., 2001). As moisture content a dominant factor in soil formation, soil horizons tend to be thicker, soil organic carbon higher, and parent material more weathered on south-facing slopes in the southern hemisphere, as shown by Bernhard et al. (2018). This could be valid for

485 Santa Gracia, La Campana, and Nahuelbuta, where precipitation events (and therefore
486 water availability) are increasing with increasing latitude, leaving the south-facing
487 hillslopes with more water and available nutrients, developing denser and taller
488 vegetation. In contrast, for Pan de Azucar, the identified pedon boundaries, GPR CO
489 profiles, and envelopes were relatively similar for north- and south-facing slopes, which
490 might be due to the fact that here almost no precipitation and no vegetation is present.
491

492 **5.4. Variations in latitude**

493 From north to south, mostly increasing regolith thicknesses have been found in the
494 key pedons (Bernhard et al., 2018; Oeser et al., 2018, see Table 1). This is roughly
495 consistent with increasing GPR signal penetration towards southern latitudes (Fig. 9,
496 Beauvais et al., 2004). An increasing trend of dielectric permittivity is as well present
497 from Pan de Azucar to Nahuelbuta (Table 2). This is probably related to increasing soil
498 water content and/or increasing organic matter and clay fraction in the soil (Bernhard et
499 al., 2018). For these reasons, the applied multi-frequency GPR approach was essential
500 for getting optimal resolution for different reflection depths and velocities (Brandt et al.,
501 2007; Orlando et al., 2016). In this way, the target boundaries could be imaged (Table
502 1), as in Pan de Azucar 1000 MHz antennae returned the highest resolution (Fig. 3 and
503 4), whereas in Nahuelbuta the deepest reflectors are visible on a 200 MHz GPR CO
504 profile at a depth of about 8 m (Fig. 7). A single frequency GPR approach might be
505 enough when measuring at one single location (e.g. Beauvais et al., 2004). However,
506 the present study shows the necessity of deploying multi-frequency GPR systems

507 depending on the subsurface targets when the spectrum of environmental parameters
508 (i.e. climate and vegetation) is broad.
509
510 **5.5. Implications of the selected study areas on the obtained results**
511 Our study focuses on a specific climate and vegetation gradient and is restricted to
512 soil-covered hillslopes, where the bedrock is made of granitic materials (Bernhard et al.,
513 2018; Oeser et al., 2018; Schaller et al., 2018). Hence, deploying geophysical methods
514 in study areas with different parent material, climate, vegetation, slope gradient, and
515 aspect, and drawing the same conclusions might be non-trivial. However, it has been
516 shown that comparable observations are valid if soil generated from a different parent
517 material is investigated, as for example basalt, gneiss, or sandstones (Befus et al.,
518 2011; Carter and Ciolkosz, 1991). Furthermore, with increasing MAP and time, the
519 influence of parent material on soil formation is negligible (Birkeland, 1984; Kutiel and
520 Lavee, 1999; Ollier and Pain, 1996). Hence, differences from this study might be more
521 evident studying in arid to hyper-arid environments than humid climates. On the other
522 hand, when rainfall is the dominant weathering process, similarities to what has been
523 found here could be expected, unless a significant slope difference is present (Leopold
524 et al., 2012).
525
526 **6. CONCLUSIONS**
527 In this study, we applied multi-frequency GPR geophysical imaging techniques to
528 characterize regolith in four locations at north and south facing slopes in the Chilean
529 Coastal Cordillera. We were able to link reflection patterns from GPR profiles with soil

data retrieved from pedons excavated in the four study areas. At the point scale, soil layering was related to reflections visible in WARRs, which were analyzed with a novel combined LMO-HMO semblance approach. For the first time, continental and aspect-related differences in GPR signals are investigated in the southern hemisphere. The primary conclusions of this study are:

1) GPR CO profiles showed both reflections and horizon interfaces shifting towards deeper depths going from north to south along the studied gradient, consistent to what was visible in the soil pedons. The same trend could be seen in the signal penetration depths of the envelope. This is interpreted to result from higher water content, organic matter, and soil thickness in the more southern study areas due to the wetter climate.

2) For the same reasons as in the previous point, south-facing hillslopes have thicker horizons and deeper boundaries visible in GPR CO profiles than their north-facing slope counterparts in each study area. This is summarized in the proposed envelope approach.

3) These latitudinal and aspect differences are negligible in Pan de Azucar study area, where no vegetation is present that could influence pedological processes, and hence give a distinct signature on obtained geophysical values.

4) The main geophysical contrast visible from GPR results could be linked with the boundary between the mobile soil and immobile saprolite layers. When present, hyperbolas indicate this heterogeneous layer interface. At some locations (La Campana and Nahuelbuta), this interface could be recognized as a continuous reflection.

553 Ongoing research in these four areas will take into account additional soil properties
554 (e.g. soil water content, texture, organic carbon), geochemical observations (e.g.
555 cosmogenic nuclides, Schaller et al. (2018)), and evolution of the studied hillslopes.
556
557 **ACKNOWLEDGEMENTS**
558 We acknowledge support from the German Science Foundation (DFG) priority
559 research program SPP-1803 “EarthShape: Earth Surface Shaping by Biota” (sub grants
560 KR 3725/1-1 and SCHA 1690/3-1), Terrestrial Environmental Observatories (TERENO),
561 and Advanced Remote Sensing-Ground-Truth Demo and Test Facilities (ACROSS). We
562 thank CONAF and all the Park Rangers for the possibility of working in the natural
563 parks, for providing access to the sample locations and help inside the National Parks.
564 We thank Maximilian Kanig and Alexis Sepulveda for helping with the geophysical
565 measurements. We thank the Editor and the Reviewers for their detailed and
566 constructive comments and suggestions that significantly improved the manuscript.
567
568 **BIBLIOGRAPHY**

569 Afshar, F.A., Ayoubi, S., Castrignanò, A., Quarto, R., Ardekani, M.R.M., 2017. Using ground-
570 penetrating radar to explore the cemented soil horizon in an arid region in Iran. Near
571 Surface Geophysics, 15, 103-110.
572 Anderson, R.S., Anderson, S.P., Tucker, G.E., 2013. Rock damage and regolith transport by
573 frost: An example of climate modulation of the geomorphology of the critical zone. Earth
574 Surface Processes and Landforms, 38, 299-316.
575 André, F. et al., 2012. High-resolution imaging of a vineyard in south of France using ground-
576 penetrating radar, electromagnetic induction and electrical resistivity tomography.
577 Journal of Applied Geophysics, 78, 113-122.
578 Aranha, P.R.A., Augustin, C.H.R.R., Sobreira, F.G., 2002. The use of GPR for characterizing
579 underground weathered profiles in the sub-humid tropics. Journal of Applied Geophysics,
580 49, 195-210.

581 Arroyo, M., Armesto, J., Squeo, F., Gutiérrez, J., 1993. Global change: The flora and vegetation
582 of Chile. Earth system response to global change: contrasts between North and South
583 America, 239-263.
584 Beauvais, A., Ritz, M., Parisot, J.-C., Bantsimba, C., Dukhan, M., 2004. Combined ERT and
585 GPR methods for investigating two-stepped lateritic weathering systems. Geoderma, 119,
586 121-132.
587 Beauvais, A., Ritz, M., Parisot, J.-C., Dukhan, M., Bantsimba, C., 1999. Analysis of poorly
588 stratified lateritic terrains overlying a granitic bedrock in West Africa, using 2-D
589 electrical resistivity tomography. Earth and Planetary Science Letters, 173, 413-424.
590 Befus, K., Sheehan, A., Leopold, M., Anderson, S., Anderson, R., 2011. Seismic constraints on
591 critical zone architecture, Boulder Creek watershed, Front Range, Colorado. Vadose
592 Zone Journal, 10, 915-927.
593 Bernhard, N. et al., 2018. Pedogenic and microbial interrelations to regional climate and local
594 topography: New insights from a climate gradient (arid to humid) along the Coastal
595 Cordillera of Chile. Catena, 170, 335-355.
596 Birkeland, P.W., 1984. Soils and geomorphology. Oxford University Press.
597 Brandt, O., Langley, K., Kohler, J., Hamran, S.-E., 2007. Detection of buried ice and sediment
598 layers in permafrost using multi-frequency ground penetrating radar: A case examination
599 on Svalbard. Remote Sensing of Environment, 111, 212-227.
600 Braun, J.-J. et al., 2009. Regolith mass balance inferred from combined mineralogical,
601 geochemical and geophysical studies: Mule Hole gneissic watershed, South India.
602 Geochimica et Cosmochimica Acta, 73, 935-961.
603 Breiner, J.M., Doolittle, J.A., Horton, R., Graham, R.C., 2011. Performance of ground-
604 penetrating radar on granitic regoliths with different mineral composition. Soil Science,
605 176, 435-440.
606 Busch, S. et al., 2013. Coupled hydrogeophysical inversion of time-lapse surface GPR data to
607 estimate hydraulic properties of a layered subsurface. Water Resources Research, 49,
608 8480-8494.
609 Butnor, J.R., Doolittle, J., Kress, L., Cohen, S., Johnsen, K.H., 2001. Use of ground-penetrating
610 radar to study tree roots in the southeastern United States. Tree physiology, 21, 1269-
611 1278.
612 Carrière, S.D., Chalikakis, K., Sénéchal, G., Danquigny, C., Emblanch, C., 2013. Combining
613 Electrical Resistivity Tomography and Ground Penetrating Radar to study geological
614 structuring of karst Unsaturated Zone. Journal of Applied Geophysics, 94, 31-41.
615 Carter, B.J., Ciolkosz, E.J., 1991. Slope gradient and aspect effects on soils developed from
616 sandstone in Pennsylvania. Geoderma, 49, 199-213.
617 Charrier, R., Ramos, V.A., Tapia, F., Sagripanti, L., 2015. Tectono-stratigraphic evolution of the
618 Andean Orogen between 31 and 37° S (Chile and Western Argentina). Geological
619 Society, London, Special Publications, 399, 13-61.
620 Cisternas, M., Martinez, P., Oyarzun, C., Debels, P., 1999. Characterization of the replacement
621 processes of native vegetation by forest plantations in a lacustrine watershed in the
622 Nahuelbuta Mountain Range, VIII Region, Chile. Revista Chilena de Historia Natural,
623 72, 661-669.
624 Davis, J.L., Annan, A.P., 1989. Ground Penetrating Radar for High-Resolution Mapping of Soil
625 and Rock Stratigraphy. Geophysical prospecting, 37, 531-551.

De Benedetto, D. et al., 2012. Integrating geophysical and geostatistical techniques to map the spatial variation of clay. Geoderma, 171, 53-63.
Dee, D.P. et al., 2011. The ERA-Interim reanalysis: Configuration and performance of the data assimilation system. Quarterly Journal of the royal meteorological society, 137, 553-597.
Di Castri, F., Goodall, D.W., Specht, R.L., 1981. Mediterranean-type shrublands. Elsevier Scientific Pub. Co.: distributors for the United States and Canada ….
Dominic, D.F., Egan, K., Carney, C., Wolfe, P.J., Boardman, M.R., 1995. Delineation of shallow stratigraphy using ground penetrating radar. Journal of Applied Geophysics, 33, 167-175.
Doolittle, J.A., Collins, M.E., 1998. A comparison of EM induction and GPR methods in areas of karst. Geoderma, 85, 83-102.
EarthShape, 2016. EarthShape: Earth Surface Shaping by Biota. www.earthshape.net.
Estrada-Medina, H., Tuttle, W., Graham, R.C., Allen, M.F., Jiménez-Osornio, J.J., 2010. Identification of Underground Karst Features using Ground-Penetrating Radar in Northern Yucatán, México. Vadose Zone Journal, 9, 653.
Fernandes, A.L., Medeiros, W.E., Bezerra, F.H.R., Oliveira, J.G., Cazarin, C.L., 2015. GPR investigation of karst guided by comparison with outcrop and unmanned aerial vehicle imagery. Journal of Applied Geophysics, 112, 268-278.
Forte, E., Pipan, M., Casabianca, D., Di Cuia, R., Riva, A., 2012. Imaging and characterization of a carbonate hydrocarbon reservoir analogue using GPR attributes. Journal of Applied Geophysics, 81, 76-87.
Fuentes, P., Díaz-Alvarado, J., Fernández, C., Díaz-Azpiroz, M., Rodríguez, N., 2016. Structural analysis and shape-preferred orientation determination of the mélange facies in the Chañaral mélange, Las Tórtolas Formation, Coastal Cordillera, northern Chile. Journal of South American Earth Sciences, 67, 40-56.
González, L. et al., 2009. Ecology and management of the Chilean Palm (Jubaea chilensis): history, current situation and perspectives. Available at http://repositorio.uchile.cl/handle/2250/120359.
Gross, R., Green, A., Horstmeyer, H., Holliger, K., Baldwin, J., 2003. 3-D georadar images of an active fault: Efficient data acquisition, processing and interpretation strategies. Subsurface Sensing Technologies and Applications, 4, 19-40.
Heincke, B., Green, A.G., Kruk, J.v.d., Horstmeyer, H., 2005. Acquisition and processing strategies for 3D georadar surveying a region characterized by rugged topography. Geophysics, 70, K53-K61.
Heincke, B., Green, A.G., Van Der Kruk, J., Willenberg, H., 2006. Semblance-based topographic migration (SBTM): A method for identifying fracture zones in 3D georadar data. Near Surface Geophysics, 4, 79-88.
Hewawasam, T. et al., 2013. Slow advance of the weathering front during deep, supply-limited saprolite formation in the tropical Highlands of Sri Lanka. Geochimica et Cosmochimica Acta, 118, 202-230.
Hirano, Y. et al., 2009. Limiting factors in the detection of tree roots using ground-penetrating radar. Plant and Soil, 319, 15.
Holbrook, W.S. et al., 2014. Geophysical constraints on deep weathering and water storage potential in the Southern Sierra Critical Zone Observatory. Earth Surface Processes and Landforms, 39, 366-380.
Jacob, R.W., Urban, T., 2016. Ground-penetrating radar velocity determination and precision estimates using common-midpoint (CMP) collection with hand-picking, semblance

672 analysis and cross-correlation analysis: a case study and tutorial for archaeologists.
673 Archaeometry, 58, 987-1002.
674 Jenny, H., 1994. Factors of soil formation: a system of quantitative pedology. Courier
675 Corporation.
676 Jol, H.M., 2008. Ground penetrating radar theory and applications. elsevier.
677 Karger, D.N. et al., 2017. Climatologies at high resolution for the earth's land surface areas.
678 Scientific data, 4, 170122.
679 Kim, J.-H., Cho, S.-J., Yi, M.-J., 2007. Removal of ringing noise in GPR data by signal
680 processing. Geosciences Journal, 11, 75-81.
681 Kukowski, N., Oncken, O., 2006. Subduction Erosion—the "Normal" Mode of Fore-Arc
682 Material Transfer along the Chilean Margin?, The Andes. Springer, pp. 217-236.
683 Kutiel, P., Lavee, H., 1999. Effect of slope aspect on soil and vegetation properties along an
684 aridity transect. Israel Journal of Plant Sciences, 47, 169-178.
685 Lehnert, L.W. et al., 2018. A Case Study on Fog/Low Stratus Occurrence at Las Lomitas,
686 Atacama Desert (Chile) as a Water Source for Biological Soil Crusts. Aerosol and Air
687 Quality Research, 18, 254-269.
688 Leopold, L.B., Wolman, M.G., Miller, J.P., 2012. Fluvial processes in geomorphology. Courier
689 Corporation.
690 Novakova, E., Karous, M., Zajíček, A., Karousova, M., 2013. Evaluation of ground penetrating
691 radar and vertical electrical sounding methods to determine soil horizons and bedrock at
692 the locality Dehtáře. Soil and Water Research, 8, 105-112.
693 Oeser, R.A. et al., 2018. Chemistry and microbiology of the Critical Zone along a steep climate
694 and vegetation gradient in the Chilean Coastal Cordillera. CATENA, 170, 183-203.
695 Ollier, C., Pain, C., 1996. Regolith, soils and landforms. John Wiley & Sons.
696 Orlando, J., Comas, X., Hynek, S.A., Buss, H.L., Brantley, S.L., 2016. Architecture of the deep
697 critical zone in the Río Icacos watershed (Luquillo Critical Zone Observatory, Puerto
698 Rico) inferred from drilling and ground penetrating radar (GPR). Earth Surface Processes
699 and Landforms, 41, 1826-1840.
700 Parsekian, A.D., Singha, K., Minsley, B.J., Holbrook, W.S., Slater, L., 2015. Multiscale
701 geophysical imaging of the critical zone. Reviews of Geophysics, 53, 1-26.
702 Rabassa, J., Clapperton, C.M., 1990. Quaternary glaciations of the southern Andes. Quaternary
703 Science Reviews, 9, 153-174.
704 Rech, J.A., Reeves, R.W., Hendricks, D.M., 2001. The influence of slope aspect on soil
705 weathering processes in the Springerville volcanic field, Arizona. Catena, 43, 49-62.
706 Schaller, M., Ehlers, T., Lang, K., Schmid, M., Fuentes-Espoz, J., 2018. Addressing the
707 contribution of climate and vegetation cover on hillslope denudation, Chilean Coastal
708 Cordillera (26°–38° S). Earth and Planetary Science Letters, 489, 111-122.
709 Scott, K., Pain, C., 2009. Regolith science. Csiro Publishing.
710 Sernageomin, 1982. Mapa Geológico de Chile. ServicioNacional de Geología y Minería
711 Santiago.
712 St. Clair, J. et al., 2015. Geophysical imaging reveals topographic stress control of bedrock
713 weathering. Science, 350, 534-538.
714 Staff, S.S., 1996. Keys to Soil Taxonomy, United States Department of Agriculture. Natural
715 Resources Conservation Service, 644.
716 Staff, S.S., 1999. Soil Taxonomy. Agriculture Handbook 436. USDA-NRCS Washington, DC,
717 USA.

718 Tillard, S., Dubois, J.-C., 1995. Analysis of GPR data: Wave propagation velocity determination.
719 Journal of Applied Geophysics, 33, 77-91.
720 van der Kruk, J., Jacob, R., Vereecken, H., 2010. Properties of precipitation-induced multilayer
721 surface waveguides derived from inversion of dispersive TE and TM GPR data.
722 Geophysics, 75, WA263-WA273.
723 van der Kruk, J., Slob, E., 2004. Reduction of reflections from above surface objects in GPR
724 data. Journal of Applied Geophysics, 55, 271-278.
725 van Overmeeren, R., 1998. Radar facies of unconsolidated sediments in The Netherlands: A
726 radar stratigraphy interpretation method for hydrogeology. Journal of Applied
727 Geophysics, 40, 1-18.
728 Walker, P., Ruhe, R., 1968. Hillslope models and soil formation. 2. Closed systems.
729 Yilmaz, Ö., 2001. Seismic data analysis: Processing, inversion, and interpretation of seismic
730 data. Society of exploration geophysicists.
731 Zaremba, N.J., Smith, C.G., Bernier, J.C., Forde, A.S., 2016. Application of Ground Penetrating
732 Radar for Identification of Washover Deposits and Other Stratigraphic Features:
733 Assateague Island, MD. Journal of Environmental and Engineering Geophysics, 21, 173-
734 186.
735 Zhao, W., Forte, E., Pipan, M., Tian, G., 2013. Ground penetrating radar (GPR) attribute analysis
736 for archaeological prospection. Journal of Applied Geophysics, 97, 107-117.
737 Zunino, S., Saiz, F., 1991. Estructura y densidad poblacional de Octodon degus Mol. Studies on
738 neotropical fauna and environment, 26, 143-148.
739
740

741 Table 1: Pedons, climate, and vegetation in the four study areas

Study areas	Pedons	Elevation [m]	A/B[1] [m]	B/C[1] [m]	C inner layering[1] [m]		bottom boundary[1] [m]	Regolith features[1]	Vegetation[2]	MAP[3] [mm/y]	MAT[3] [°C]
Pan de Azucar	S-top (AZPED60)	367	0.05	0.20	0.53	-	-	0-0.20 m: 1 cm clasts 0.20-0.45 m: fractured blocks (5-10 cm) 0.45- m: fractured blocks (20 cm)	None	15	20.1
	S-mid (AZPED50)	364	0.05	0.20	0.55	0.80	1.60				
	S-toe (AZPED40)	361	0.07	0.25	0.45	0.80	1.25				
	N-mid (AZPED21)	376	0.05	0.20	0.30	0.45	1.10				
Santa Gracia	S-top (SGPED20)	740	0.05	0.35			1.15	0-0.30 m: clasts (2 mm), roots (1 cm) 0.30- m: fractured blocks (5-20 cm)	Shrubs and cacti	77	15.1
	S-mid (SGPED40)	709	0.35	0.60	0.75		2.05				
	S-toe (SGPED60)	668	0.35	0.50	0.80		2.1				
	N-mid (SGPED70)	711	0.20	0.35	0.42		2.00				
La Campana	S-top (LCPED10)	757	0.05	0.40	-		0.68	0-0.20 m: 2 mm particles 0.20- m: fractured blocks (10-20 cm), roots (5 cm)	Mediterranean, shrubs, and sclerophyllous trees	326	14.9
	S-mid (LCPED20)	747	0.30	0.60	-		1.85				
	S-toe (LCPED30)	735	0.20	0.60	-		3.65				
	N-mid (LCPED40)	748	0.15	0.45	1.00		1.40				
Nahuelbuta	S-top (NAPED10)	1270	0.45	0.70	0.90		2.05	0-1.00 m: clasts (1-10 cm), roots (2 cm) 1.00- m: fractured blocks (10-20 cm)	Humid temperate forest with *Araucaria araucana* and *Nothofagus sp* trees	1050	12.9
	S-mid (NAPED20)	1250	0.50	1.00	-		2.04				
	S-toe (NAPED30)	1227	0.55	0.85	0.90		1.15				
	N-mid (NAPED40)	1226	0.40	0.85	-		2.00				

[1]Depth of horizons from Bernhard et al. (2018); Oeser et al. (2018)
[2]Vegetation data from Arroyo et al. (1993)
[3]Mean annual precipitation (MAP) and temperature (MAT) from Karger et al. (2017)

747 Table 2: Values of geophysical parameters for south- and north-facing hillslopes in the four study areas

Study areas	Aspect	GW velocity[1] [m/ns]	ε_r[2]	avg energy 55-60 ns[3]	Maximum travel time[4] [ns]	Penetration depth[4] [m]	Dominant GPR wavelength λ[5] [m]			Total GPR measurements length [km]
							200 MHz	500 MHz	1000 MHz	
Pan de Azucar	S-facing	0.147 ± 0.003	3.95	$2.74*10^{11}$	26.8	1.97	0.74	0.29	0.14	1.23
	N-facing			$2.75*10^{11}$	22.6	1.66				
Santa Gracia	S-facing	0.153 ± 0.006	3.59	$2.89*10^{11}$	24.6	1.81	0.77	0.31	0.15	1.58
	N-facing			$2.86*10^{11}$	16.4	1.21				
La Campana	S-facing	0.134 ± 0.011	4.98	$2.83*10^{11}$	28.4	2.09	0.68	0.27	0.14	0.48
	N-facing			$2.85*10^{11}$	16.4	1.21				
Nahuelbuta	S-facing	0.115 ± 0.006	6.26	$1.31*10^{12}$	45.2	3.32	0.58	0.23	0.12	0.38
	N-facing			$3.33*10^{12}$	37.4	2.75				

748

749 [1]Average ground wave velocities in each study areas obtained from WARR measurements
750 [2]Relative dielectric permittivity for each location derived from the average ground wave velocity
751 [3]Average GPR energy for the north- and south-facing envelopes in each study area in the travel time range between 55 and 60 ns multiplied by a factor of 3
752 [4]Maximum travel times and penetration depths derived from the envelope in north- and south-facing slopes in each study areas
753 [5]Dominant wavelength within each location calculated using the average ground wave velocity and the deployed GPR central frequency

754

List of Figures

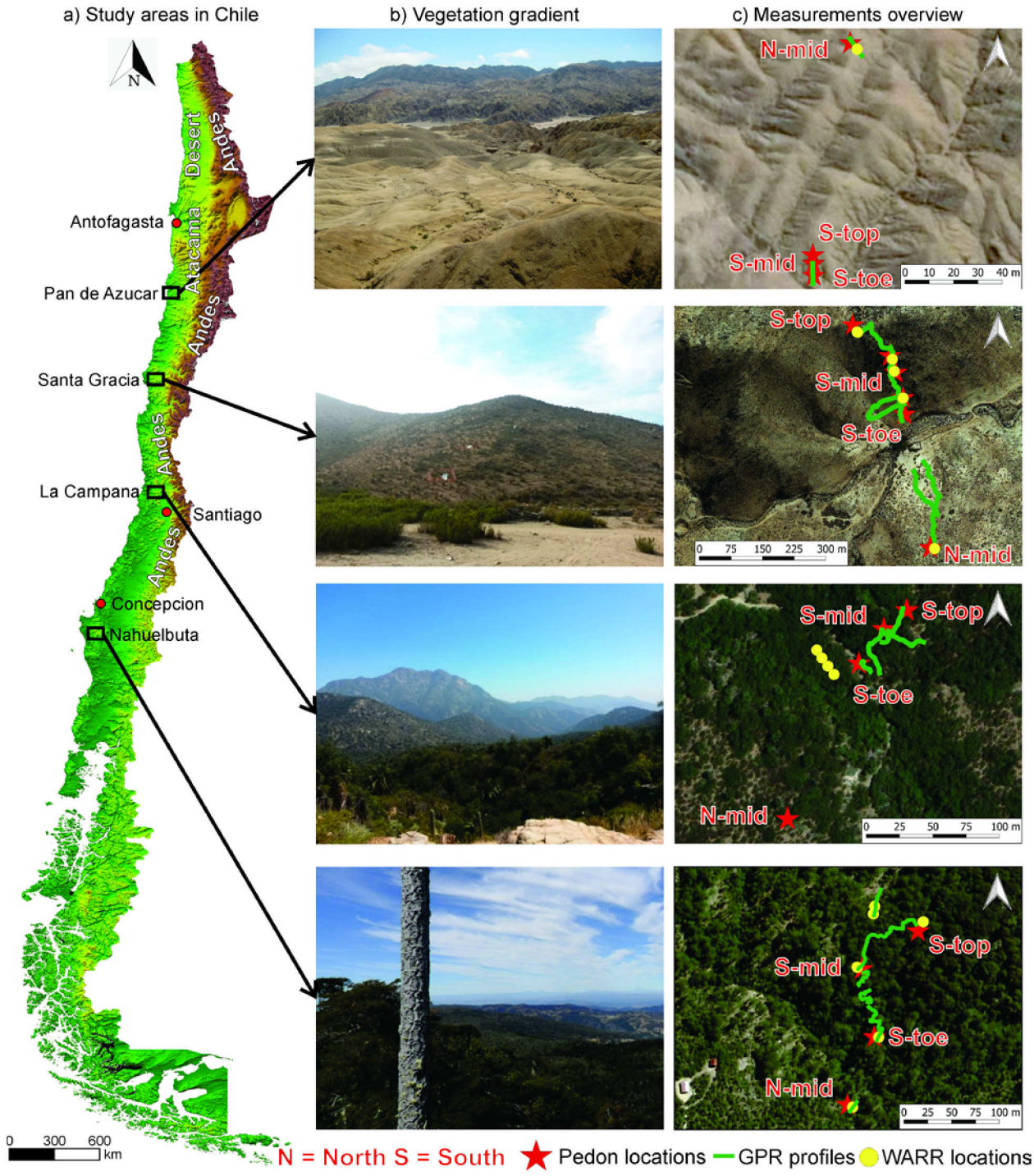

Fig. 1: a) Map with the four study areas along the Chilean Coastal Cordillera (black rectangles). From north to south are the study areas Pan de Azucar, Santa Gracia, La Campana, and Nahuelbuta. b) Denser vegetation is observed from north to south in

latitude. c) In the overview maps, locations of the pedons are indicated by red stars. GPR CO profiles and WARRs are indicated by green lines and yellow circles. Specific locations shown in the text are indicated by blue arrows and labels.

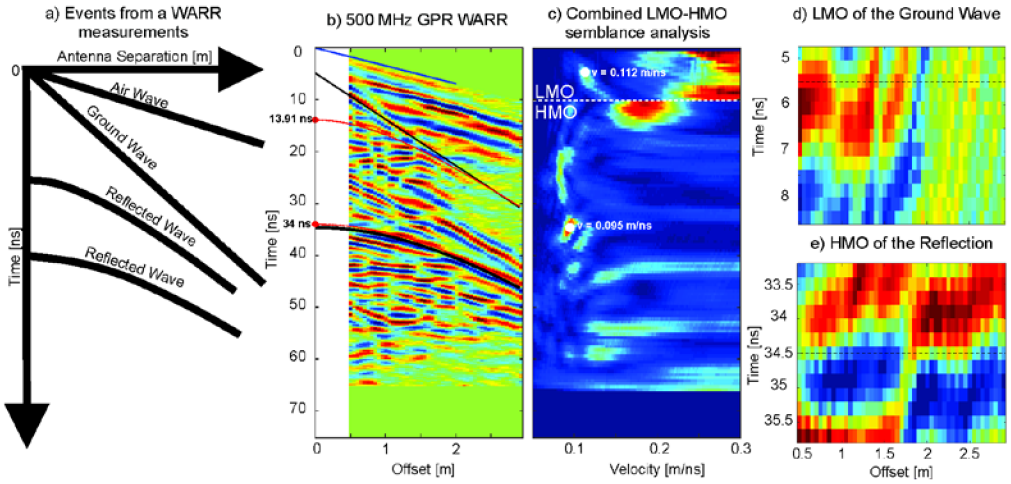

Fig. 2: Novel combined LMO-HMO approach for the velocity analysis of ground and reflected waves. a) Theoretical wave trajectories for air wave, ground wave, and reflections in a WARR measurements. b) WARR profile for 500 MHz antennae from Nahuelbuta study area. The ground wave and one reflection (black hyperbola) have been picked. The red hyperbolas represent theoretical signal produced by known soil layers at a known depth. c) The white dashed line separates LMO and HMO semblance panels. The white circles indicate the picked velocities of the ground wave and the reflection. d) And e) semblance window widths (see Eq. 1) after the move-out correction for the picked velocities. d) Shows the linear move-out correction for the ground wave picking; e) shows the hyperbolic move-out correction for the reflection. Red color and blue color indicate positive and negative amplitudes, respectively. The WARR data were measured in Nahuelbuta south-facing mid slope (see Fig. 1c).

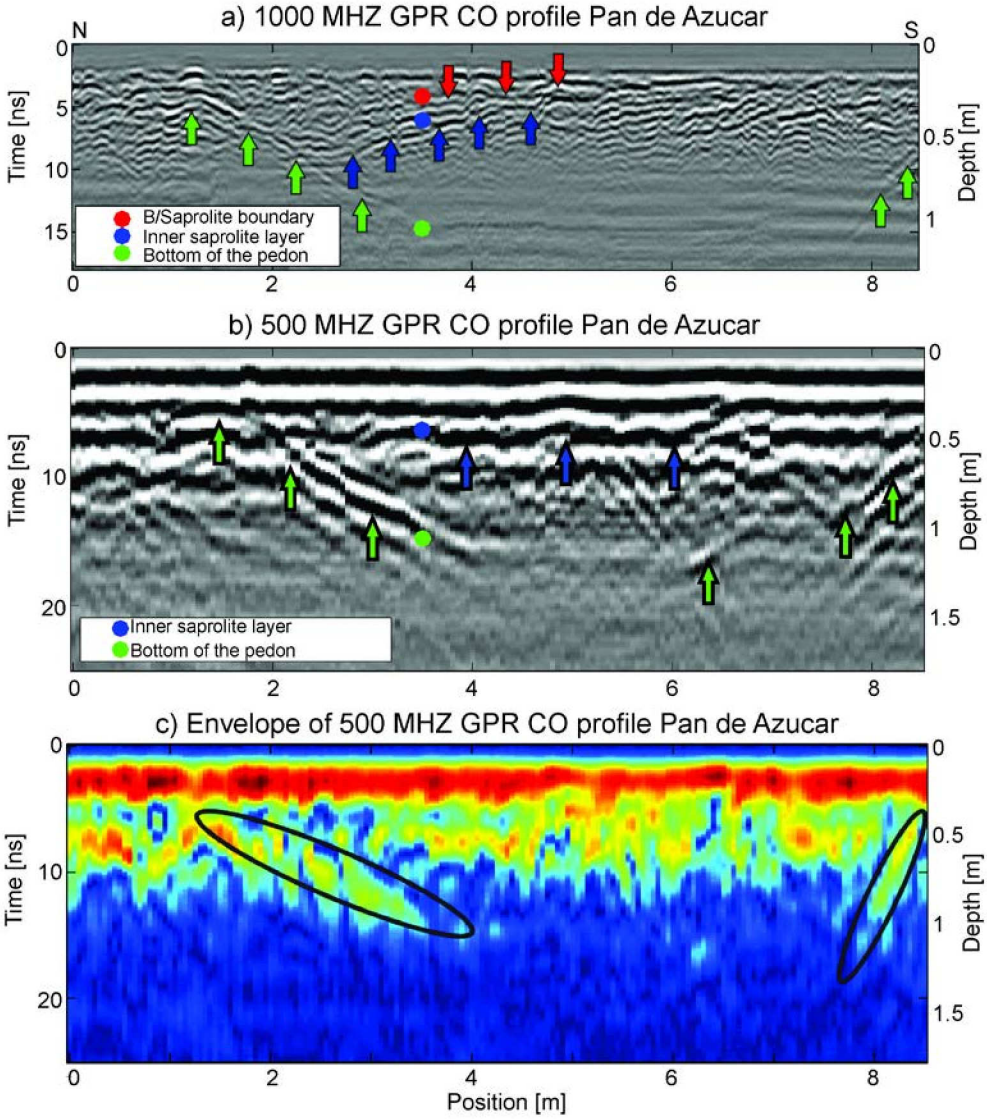

776

777 Fig. 3: Common-offset (CO) profiles along the north-facing mid pedon in Pan de Azucar
778 study area measured with a) 1000 MHz and b) 500 MHz GPR antennae. In a) a
779 background removal was applied to remove horizontal noise in the later travel times. c)
780 Reflection strength (envelope) of the profile in b), where red color indicates high
781 reflectivity values and blue color low reflectivity values. Arrows indicate continuous
782 reflections linked with the correspondent color boundary.

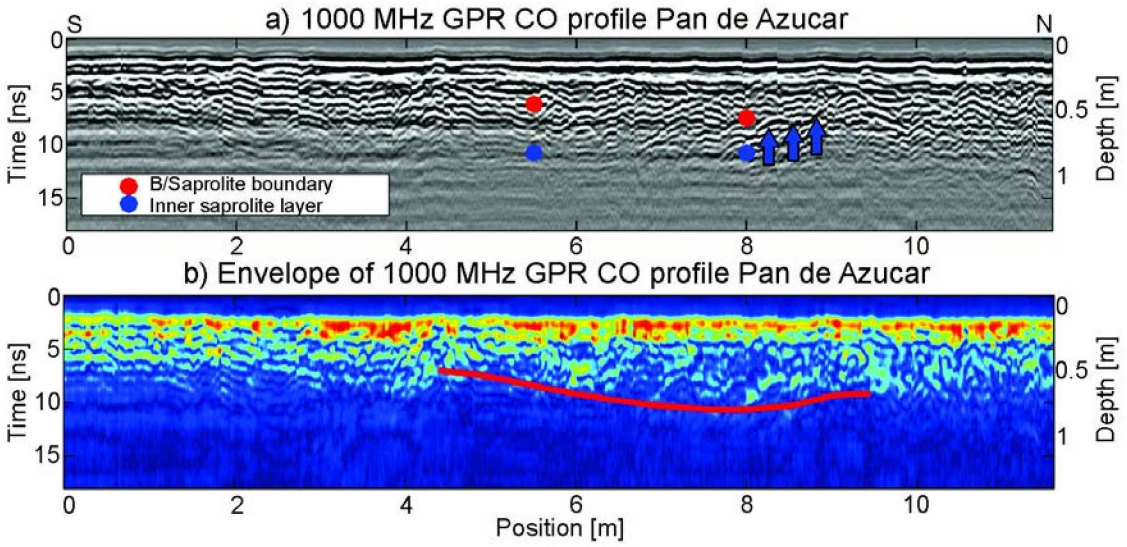

783

784 Fig. 4: a) GPR CO profile measured with 1000 MHz antennae over the south-facing
785 hillslope of Pan de Azucar study area, where layering from toe pedon (left) and mid
786 pedon (right) is plotted. b) Shows the envelope of the GPR profile in a). The red line
787 indicates the variation in signal penetration along the profile.

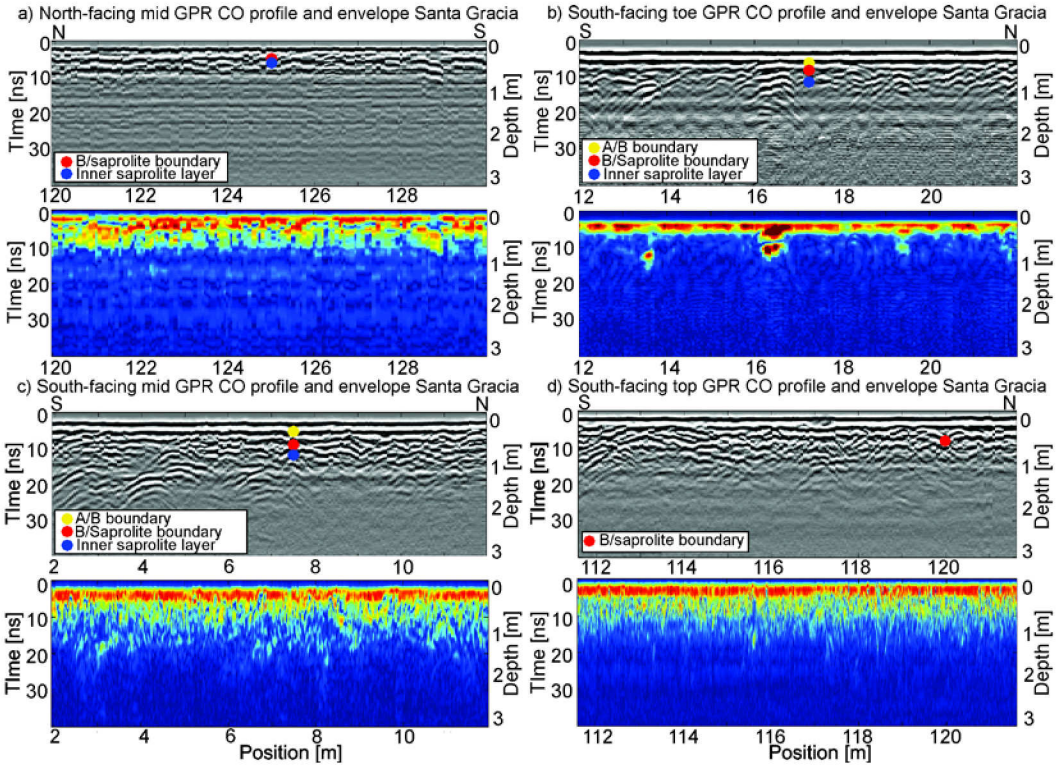

788

789 Fig. 5: Four parts of GPR CO profiles from Santa Gracia measured on a) north-facing
790 mid pedon, b) south-facing toe pedon, c) south-facing mid pedon, and d) south-facing
791 top pedon. The envelope is plotted alongside each profile.

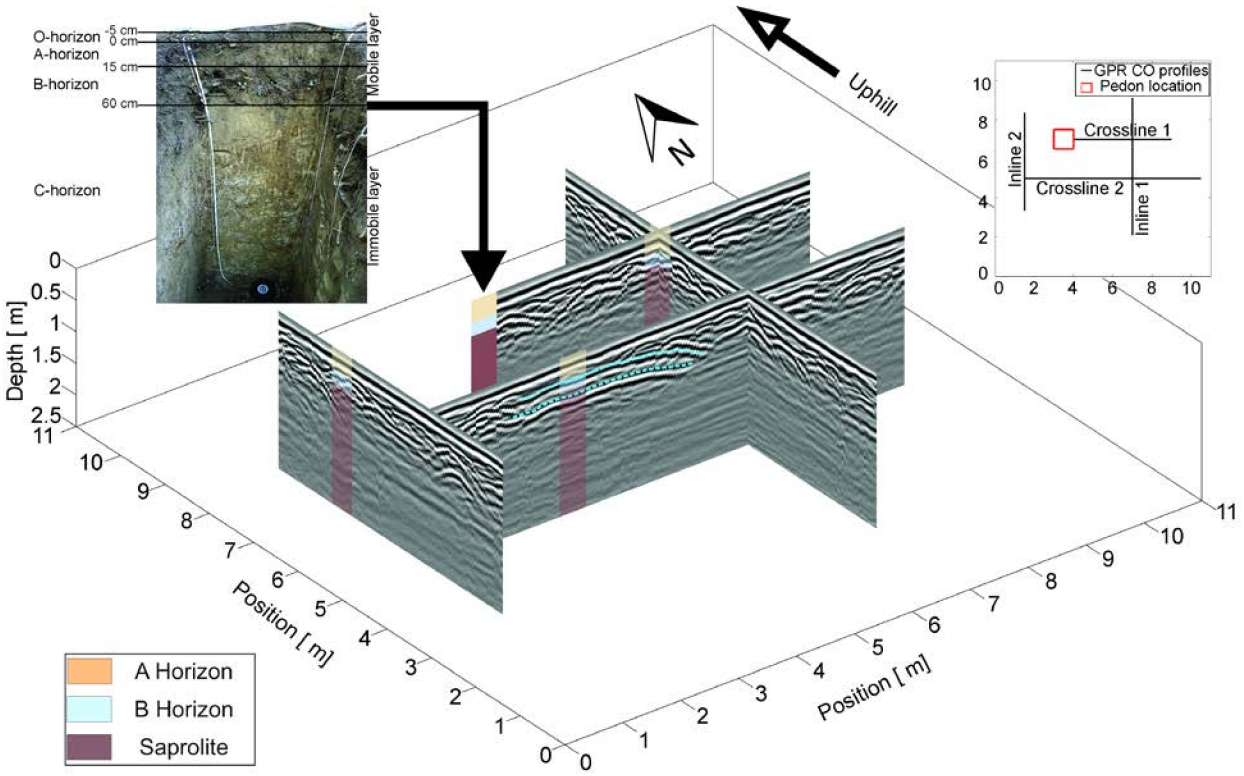

792

793 Fig. 6: 2.5D combined 500 MHz GPR CO inlines and crosslines measured around the
794 mid pedon (indicated by the black arrow) of south-facing hillslope in La Campana study
795 area. The layering visible in the pedon was superimposed in transparency on the
796 profiles as shown. The cyan dashed lines indicate continuous reflections.

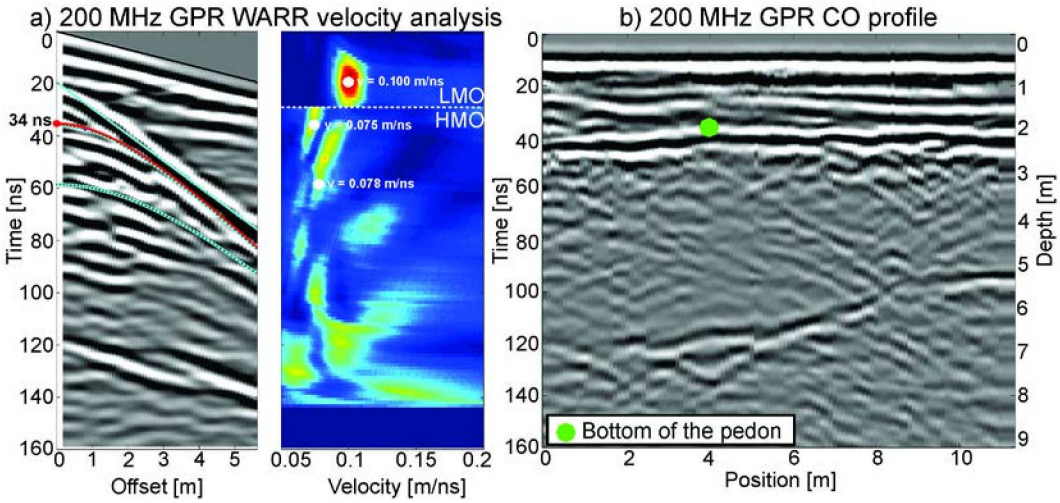

797

798 Fig. 7: a) 200 MHz GPR WARR measured at the south-facing mid pedon in Nahuelbuta
799 study area. Cyan trajectories indicate picked velocities in the semblance panel; the red
800 hyperbola indicates the theoretical signal produced by the pedon bottom boundary. b)
801 200 MHz GPR CO profile measured along the south-facing hillslope mid pedon in
802 Nahuelbuta study area. The green dot indicates the bottom of the pedon. It fits with a
803 high-amplitude continuous reflector at a depth of around 40 ns (2 m).

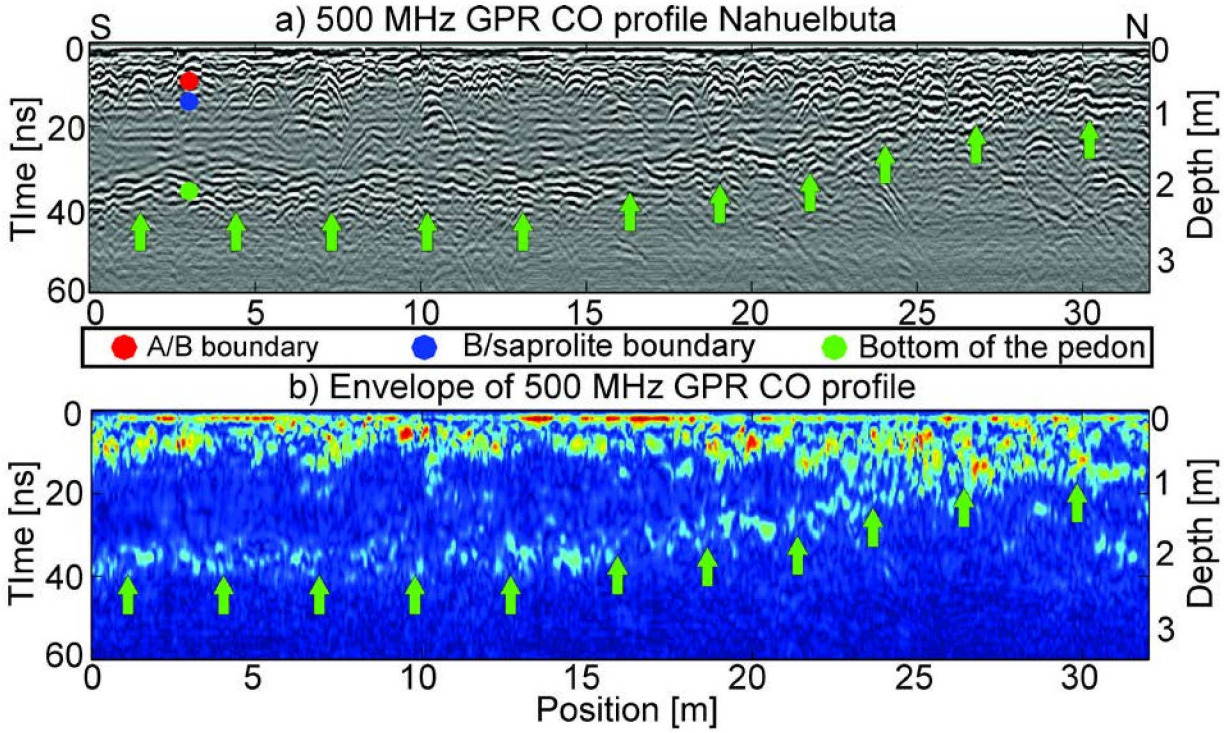

804

Fig. 8: a) 500 MHz GPR CO profile along the south-facing mid pedon in Nahuelbuta study area. Arrows indicate continuous reflections linked with the correspondent color boundary. b) Envelope of the 500 MHz GPR CO profile, color between yellow and red indicates high reflectivity. Green arrows indicate the reflectivity associated with the reflection related to the bottom of the pedon boundary.

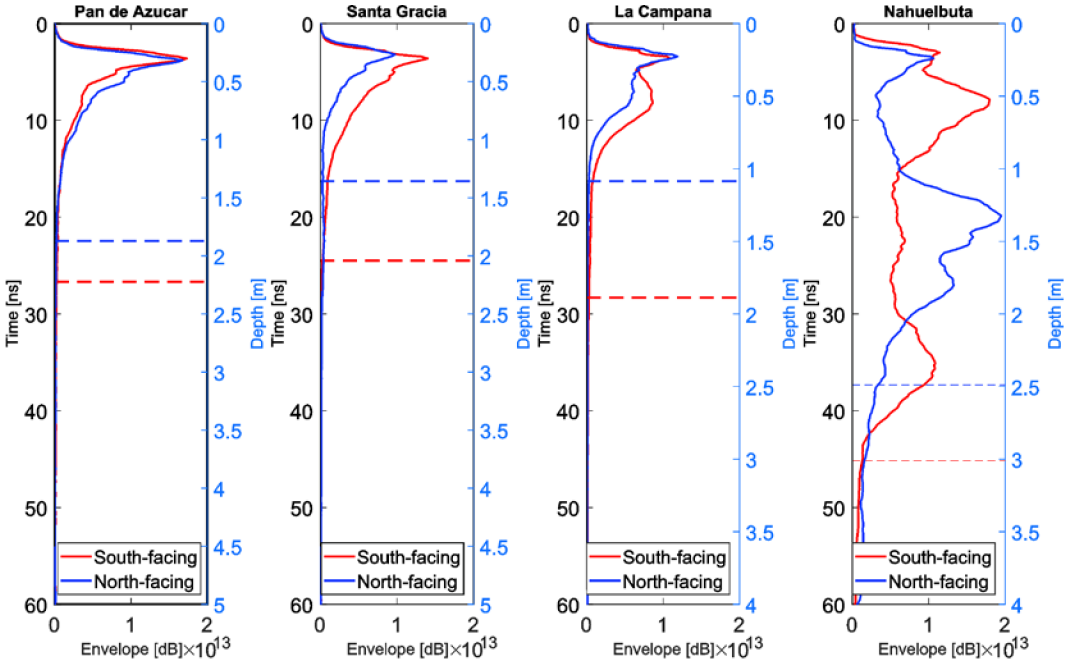

Fig. 9 Average envelopes for north- and south-facing mid slopes in the four study areas. The horizontal dashed lines correspond to the calculated signal-to-noise thresholds.

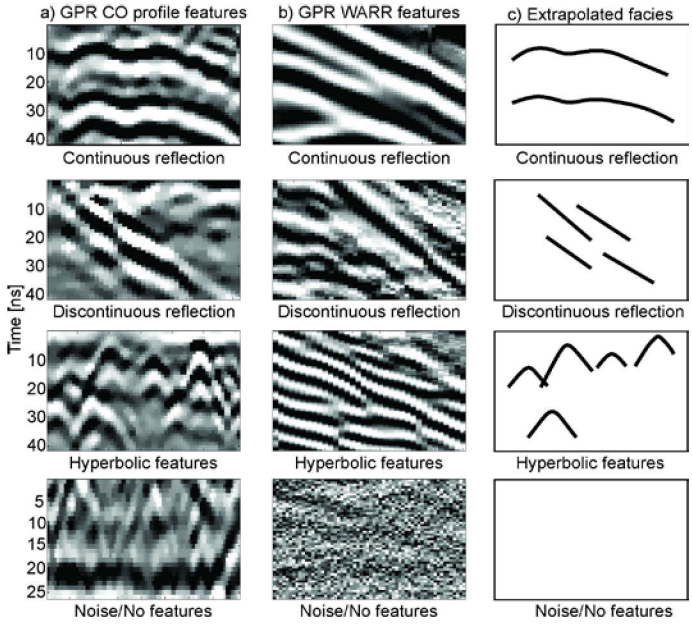

Fig. 10 Main GPR reflection patterns classified as 1) continuous reflections, 2) discontinuous reflections, 3) hyperbolic features, and 4) no clear reflection recognizable in a) GPR CO profiles, b) GPR WARR measurements, and c) indicated as facies.

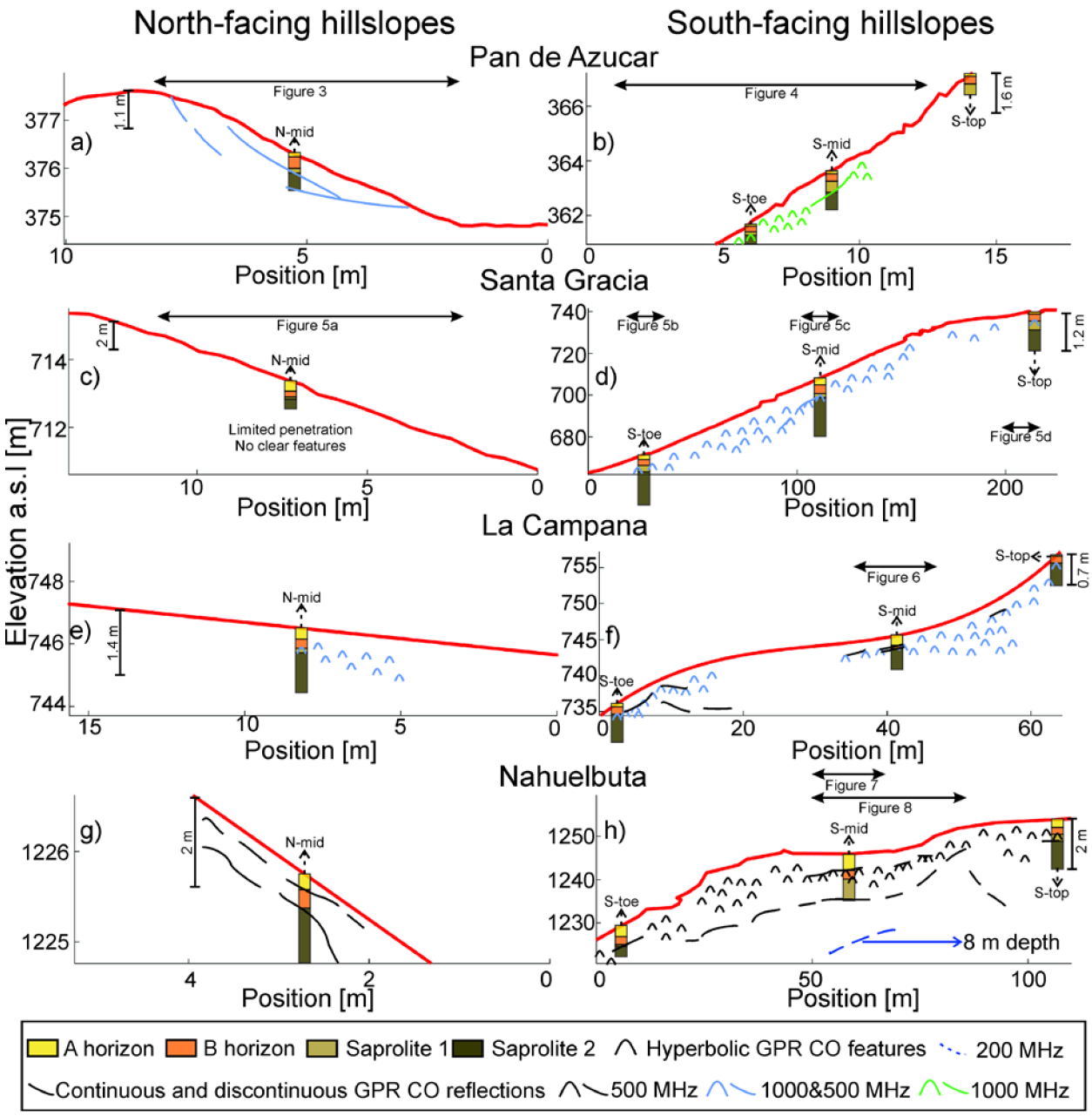

817

818 Fig. 11: Red lines show topography obtained at the north-facing and south-facing slopes
819 in a) and b) Pan de Azucar, c) and d) Santa Gracia, e) and f) La Campana, and g) and
820 h) Nahuelbuta, respectively. On each slope, the excavated pedons have been plotted
821 with the layering indicated in the legend. The scale of pedons and GPR features is
822 exaggerated as indicated by the axis on the top of each hillslope. Hyperbolic features
823 and (dis-)continuous reflections recognized in the GPR profiles have been drawn to

824 enable a correlation between layer boundaries and geophysical information. Horizontal
825 black arrows indicate the positions where GPR profiles shown in the results were
826 measured.